Optical and Quantum Electronics (2006) 38:761–780
DOI 10.1007/s11082-006-9024-x

Self-phase modulation in slow-wave structures: A comparative numerical analysis

FRANCESCO MORICHETTI[1,*], ANDREA MELLONI[1], JAROSLAV ČÁP[2], JIŘÍ PETRÁČEK[2], PETER BIENSTMAN[3], GINO PRIEM[3], BJORN MAES[3], MICHELE LAURITANO[4], AND GAETANO BELLANCA[4]

[1] *Dipartimento di Elettronica e Informazione, Politecnico di Milano, via Ponzio 34/5, 20133 Milano, Italy*
[2] *Institute of Physical Engineering, Brno University of Technology Technická 2, 616 69 Brno, Czech Republic*
[3] *Department of Information Technology, Ghent University, Sint-Pietersnieuwstraat 41, 9000 Ghent, Belgium*
[4] *Dipartimento di Ingegneria, Università di Ferrara, Via Saragat 1, 44100 Ferrara, Italy*
*(*author for correspondence: E-mail: morichetti@elet.polimit.it)*

Received 21 July 2006; Accepted 3 November 2006

Abstract. Self-phase modulation effects in 1D optical slow-wave structures made of Fabry–Pérot cavities coupled by Distributed Bragg Reflectors (DBRs) are discussed. The nonlinear response of the structure is investigated by a comparative analysis of several numerical methods operating either in time or frequency-domain. Time-domain methods include two Finite-Difference Time-Domain approaches, respectively, optimized to compensate for numerical dispersion and to model nonlinearity at any order. In the frequency-domain an efficient method based on a numerical integration of Maxwell's equations and an iterative nonlinear extension of the Eigenmode Expansion method are discussed. A Nonlinear Equivalent Circuit of DBRs is also presented as a useful model to reduce computational efforts. Numerical results show that bistable effects and self-pulsing phenomena can occur when either the optical power or the number of coupled cavities of the structure are sufficiently increased.

Key words: Nonlinear optics, optical bistability, resonators, self-phase modulation, slow-wave propagation

1. Introduction

Optical resonators have been subject to increasing interest in the last years because they are considered promising devices for many linear and nonlinear applications. For instance, it has been experimentally shown that the efficiency of all-optical switches (Heebner *et al.* 2004) and all-optical wavelength converters (Absil *et al.* 2000) can be increased by several orders of magnitude when the process is assisted by a resonator. It has been also shown that the bandwidth limitations of a single resonator can be substantially reduced by cascading many optical resonators in such a way to build up a slow-wave struture (SWS) (Melloni *et al.* 2003a), while preserving all the benefits given by optical resonances. Inside a SWS the group velocity of an optical wave is reduced as much as the finesse of the cavities is high

and this effect is responsible for the enhancement of self-phase modulation (SPM) effects (Chen *et al.* 2003; Melloni *et al.* 2003b) as well as frequency mixing phenomena of optical signals at different wavelengths (Xu *et al.* 2000; Melloni *et al.* 2003c; Blair 2005).

The interplay of nonlinearities with the amplitude and phase spectral response of SWSs leads to a variety of phenomena, not easily predictable analytically, so that accurate modeling techniques and efficient numerical methods are required for a detailed analysis in nonlinear regime. For these structures, computational time of conventional numerical methods typically increases at frequencies close to cavity resonances, because of the strong enhancement of group delay and intra-cavity optical power, both boosting nonlinearity.

This paper focuses on the modelling and numerical investigation of SPM effects in One-dimensional (1D) optical SWSs consisting of Fabry–Pérot cavities filled with a Kerr medium and coupled each other by distributed bragg reflectors (DBRs). A comparative analysis of several numerical methods operating either in time or frequency-domain is provided. The structure under investigation was proposed in the framework of COST P11 action and is described in Sect. 2. Three time-domain methods are presented in Sect. 3. The first one is a Phase Velocity Corrected nonuniform Finite Difference Time-Domain (PVC-FDTD) method developed to compensate for numerical dispersion problems in conventional FDTD schemes; the second is a FDTD method based on a nonlinear and dispersive Lorentz–Maxwell (LM-FDTD) model to take into account both material dispersion and nonlinearity at any order; the third method models the DBRs of the Fabry-Pérot cavities by means of a nonlinear equivalent circuit (NEC), which is used to significantly reduce computational efforts in time-domain simulations (NEC-TD). Two frequency-domain approaches are discussed in Sect. 4, based, respectively, on a numerical integration of Maxwell's equations in the frequency-domain (NI-FD) after a suitable transformation into coupled ordinary differential equations and an iterative nonlinear extension of the Eigenmode Expansion (NEME-FD) method. Sect. 5 presents numerical results and explanations of phenomena observed in these structures, such as optical bistability and self-pulsing. The accuracy, computational efficiency, versatility and limits of the proposed techniques are analyzed, compared and discussed in Sect. 6.

2. Slow wave structures

The SWS under investigation, proposed in the framework of COST P11 action, is sketched in Fig. 1. It consists of N one dimensional Fabry–Pérot cavities, with optical length $\lambda_0 = 1550\,\text{nm}$, coupled each other by means of

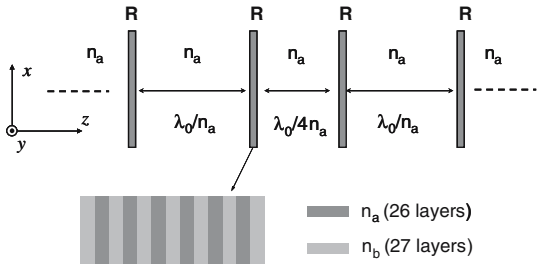

Fig. 1. Schematic of the SWS under investigation.

an intermediate quarter-wave layer. Each partial reflector R consists of a DBR including 27 layers of refractive index n_b=2.36 interleaved with 26 layers of refractive index $n_a = 2.6$. The medium filling the cavities has refractive index n_a.

The optical field propagates in the z-direction, with electric and magnetic field oriented in the x- and y-direction, respectively, and $\exp(j\omega t)$ time dependence convention is assumed. Both the DBR and the intra-cavity medium posses a Kerr nonlinearity so that the total refractive index of the SWS is given by

$$n(z, |E_x|^2) = n_0(z) + n_2 |E_x(z)|^2 , \tag{1}$$

where $n_0(z)$ is the linear refractive index (n_a or n_b) and $n_2 = 2.4 \times 10^{-16}\,\mathrm{cm}^2/\mathrm{V}^2$ is the Kerr nonlinear index, assumed constant along the whole structure. The aim of this work is to investigate, both in time and frequency-domain, the nonlinear response of the SWS for increasing number N of cavities and increasing input power level. Even though material dispersion is typically high in high-index nonlinear materials, in this paper it is neglected in view of the strong dispersion of the structure. However, all the presented methods either include or can be straightforwardly extended to take into account also the effects of material dispersion.

3. Time-domain methods

In this section a brief description of three time-domain numerical methods used to investigate the nonlinear response of SWSs are described. The first one is a FDTD approach in which numerical dispersion is compensated by a Phase Velocity Corrected nonuniform algorithm (PVC-FDTD); the second method allows to model the SWS nonlinear response at any order, including material dispersive behavior, by means of a nonlinear Lorentz-Maxwell model for FDTD; the third method proposes a NEC of nonlinear

DBRs, useful to significantly reduce the spatial grid in time-domain simulation (NEC-TD) so as to speed up computational time.

3.1. PHASE VELOCITY CORRECTED NONUNIFORM FDTD (PVC-FDTD)

The accuracy of the FDTD method, originally formulated by Yee (1966), strongly depends on the mesh density and the time step used for calculation. The main source of errors in the FDTD algorithm is numerical dispersion which causes a deceleration of numerical phase velocity. To eliminate this effect, that originates an artificial shift of the spectral response of resonant structures, like the SWS under investigation, a phase velocity corrected algorithm (Christ *et al.* 2002) was adopted and suitably extended to the nonlinear regime.

The fields are discretized in space and time using $[z_i, t_n]$ mesh points. Considering the dielectric medium without electric and magnetic losses, the E-field and H-field update equations can be written as (Christ *et al.* 2002)

$$E_x|_i^{n+1} = E_x|_i^n + cb_{1i}\ H_y\big|_{i+\frac{1}{2}}^{n+\frac{1}{2}} - cb_{2i}\ H_y\big|_{i-\frac{1}{2}}^{n+\frac{1}{2}}, \tag{2}$$

$$H_y\big|_{i+\frac{1}{2}}^{n+\frac{1}{2}} = H_y\big|_{i+\frac{1}{2}}^{n-1/2} + db_i\left(E_x|_{i+1}^n - E_x|_i^n\right), \tag{3}$$

where the update coefficients have the form

$$cb_{1i} = -\frac{2Z_i \sin\left(\frac{\omega_0 \Delta t}{2}\right) \cos\left(\frac{k_i \Delta z_{i-1}}{2}\right)}{X_i}, \tag{4}$$

$$cb_{2i} = -\frac{2Z_i \sin\left(\frac{\omega_0 \Delta t}{2}\right) \cos\left(\frac{k_{i-1} \Delta z_i}{2}\right)}{X_i}, \tag{5}$$

$$X_i = \sin\frac{k_i \Delta z_i}{2} \cos\frac{k_i \Delta z_{i-1}}{2} + \sin\frac{k_i \Delta z_{i-1}}{2} \cos\frac{k_i \Delta z_i}{2}, \tag{6}$$

$$db_i = -\frac{\sin\left(\frac{\omega_0 \Delta t}{2}\right)}{Z_i \sin\left(\frac{k_i \Delta z_i}{2}\right)}. \tag{7}$$

In Eqs. (4)–(7), Z_i is the wave impedance of the medium, k_i is the wave number for the frequency ω_0 in the cell indexed i, ω_0 being the optimization frequency for which the FDTD algorithm works completely dispersionless. Z_i and k_i depend on the refractive index $n|_i$, which is modeled by

$$n|_i = n_0|_i + n_2|_i \left(\max |E_x|_i^{DT}\right)^2, \tag{8}$$

where $\max |E_x|_i^{DT}$ is a maximum absolute value of the E-field found in the cell i over the time $DT = 2\lambda \max [n_0(z)]/c$.

Note that the update coefficients are evaluated only once in every time section DT rather then in each time step and this feature considerably decreases computational time.

3.2. THE NONLINEAR LORENTZ–MAXWELL FDTD MODEL

The nonlinear and dispersive Lorentz–Maxwell FDTD model includes material dispersion in order to reduce the phase matching of undesired frequency conversion processes, thus allowing to select the dominant parametric interaction, such as Kerr effect in respect to third harmonic generation. The physical model implemented here, with a single resonance at ω_r (multiple resonances can easily be added using a better Sellmeier representation of the material dispersion), is the same originally presented for the study of quadratic nonlinearity in (Lauritano *et al*. 2006) and is described by the following set of equations,

$$\begin{aligned}
&\frac{\partial H_y}{\partial t} = -\frac{1}{\mu_0}\left(\frac{\partial E_x}{\partial z}\right),\\
&\frac{\partial E_x}{\partial t} = -\frac{1}{\epsilon_0\epsilon_\infty}\left(\frac{\partial H_y}{\partial z} + \frac{\partial P_x}{\partial t}\right),\\
&\frac{\partial^2 P_x}{\partial t^2} + \gamma_0\frac{\partial P_x}{\partial t} + \omega_r^2\left(P_x + aP_x^2 + bP_x^3 + \cdots\right) = \omega_r^2\epsilon_0\left(\epsilon_S - \epsilon_\infty\right)E_x,
\end{aligned} \tag{9}$$

where E_x, H_y, and P_x are electric, magnetic, and polarization effective components, respectively, whereas ϵ_S and ϵ_∞ are dielectric constants at zero and infinite frequency, respectively, and γ_0 accounts for frequency-dependent dielectric losses. The $a, b, \ldots$ coefficients can be expressed in terms of physical nonlinear susceptibilities $\chi^{(n)}$ through multiscale expansion (Boyd 1992). For instance, in case of a centrosymmetric crystal only third order non linearity is taken into account and the two lowest order coefficients become

$$a = 0, \qquad b = -\frac{\chi^{(3)}}{\epsilon_0^2(\epsilon_S - \epsilon_\infty)^3}. \tag{10}$$

In this technique, both numerical dispersion and material dispersion are compensated by considering the overall effective dispersion. Compared with standard FDTD schemes (Joseph and Taflove 1997), the present approach has two main advantages: first it allows to model the nonlinear response at any order by adding the appropriate power of P_x in Equation 9); second, approximating derivatives with central differences (following Yee relations (Taflove 1995)), yields a direct (noniterative) scheme.

3.3. TIME-DOMAIN METHOD USING THE NONLINEAR EQUIVALENT CIRCUIT OF A DBR (NEC–TD)

The complexity of the structure as well as computational efforts can be greatly reduced by replacing every DBR of the SWS with a suitable NEC. The NEC proposed here is an extension of the equivalent circuit of the linear Bragg grating proposed by some of the authors in a previous contribution (Melloni *et al.* 2003d). The novelty is that in the NEC the nonlinearity of the DBR is taken into account and its impact on the SWS nonlinear response is correctly evaluated. Even though the model can be applied at every wavelength, for clarity's sake the treatment is here conveniently restricted to a first-order approximation around the Bragg wavelength λ_B of the DBR and to dispersionless media.

3.3.1. *The nonlinear equivalent circuit of a DBR*

Figure 2a schematically shows the NEC of a DBR, consisting of a concentrated mirror with field reflectivity r and transmissivity jt, placed between two equivalent lengths L_e. The transmission matrix $\mathbf{T}_e$ of the equivalent circuit relating the complex amplitude of the waves at the right $A^{\pm}(0)$ of the NEC to those at the left $A^{\pm}(L)$, is simply

$$\mathbf{T}_e = \frac{j}{t}\begin{bmatrix} -\exp(j2\varphi_e) & r \\ -r & \exp(\mathrm{j}2\varphi_e) \end{bmatrix}, \tag{11}$$

where $\varphi_e = 2\pi n_0 L_e/\lambda$, n_0 being a convenient reference refractive index, assumed equal to n_a in the following of the paper. The expressions of r, t, and L_e can be derived by equating the elements of the matrix $\mathbf{T}_e$ to those of the DBR transmission matrix, which can be known analytically, as in the case of a uniform DBR, or more generally by numerical computations or experimentally. From this equivalence the expression of the equivalent length of the DBR is obtained (Melloni *et al.* 2003d),

$$L_e = L_{eB} + \Delta L_e \frac{\lambda - \lambda_B}{\lambda_B}, \tag{12}$$

where $L_{eB} = L/2 \pm \Lambda/4$ is the equivalent length at λ_B, with Λ the DBR period. The parameter $\Delta L_e = L_{eB} - r_M/2\kappa_g$ is the slope of the equivalent length at λ_B, with (Stignani 2001)

$$\kappa_g = \frac{4}{\lambda_B}\frac{n_a n_b}{n_a + n_b}\ln\left(\frac{n_a}{n_b}\right) \tag{13}$$

the grating coupling coefficient at λ_B and $r_M = \tanh(\kappa_g L)$ the maximum field reflectivity.

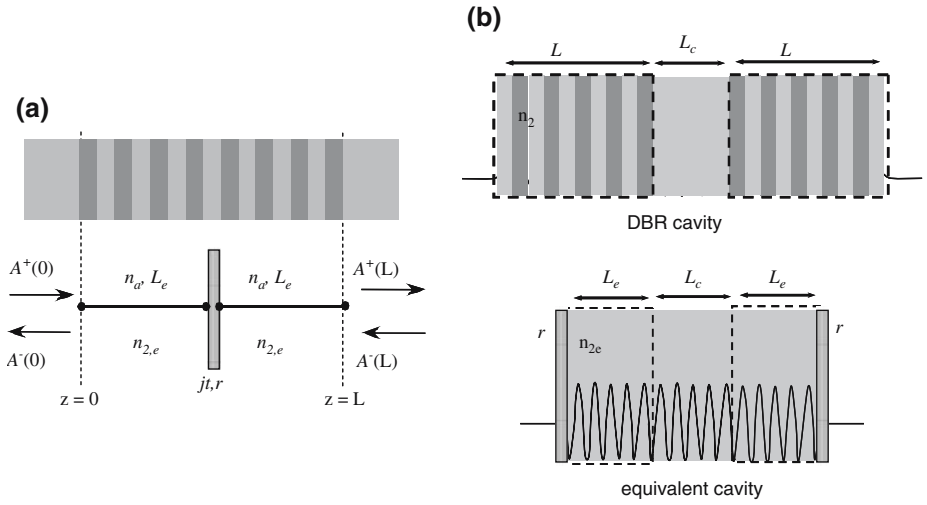

Fig. 2. (a) Nonlinear equivalent circuit of a DBR and (b) its application to a Fabry–Pérot cavity.

In nonlinear regime, the optical field distribution inside the DBR has to be evaluated to correctly model the response of the SWS. The expression of the forward and backward wave in the grating at the Bragg wavelength are, respectively (Yariv and Yeh, 1984)

$$A^{+}(z) = A^{+}(0)\frac{\cosh[\kappa_{\mathrm{g}}(L-z)]}{\cosh(\kappa_{\mathrm{g}}L)},\ A^{-}(z) = jA^{+}(0)\frac{\sinh[\kappa_{\mathrm{g}}(L-z)]}{\cosh(\kappa_{\mathrm{g}}L)}, \tag{14}$$

where L is the DBR geometrical length and z indicates the distance from the input section. It is possible to define an effective nonlinear length of the DBR for either the forward and the backward field as

$$L_{\mathrm{NL}}^{\pm} = \frac{1}{|A^{+}(0)|^2}\int_0^L |A^{\pm}(z)|^2 \mathrm{d}x = \frac{\tanh(\kappa_{\mathrm{g}}L)}{2\kappa_{\mathrm{g}}} \pm \frac{L}{2\cosh^2(\kappa_{\mathrm{g}}L)}. \tag{15}$$

The overall nonlinear effective length of the grating is $L_{\mathrm{NL}} = L_{\mathrm{NL}}^{+} + L_{\mathrm{NL}}^{-} = \tanh(\kappa_{\mathrm{g}}L)/\kappa_{\mathrm{g}}$ and it rigorously expresses the length of a homogeneous medium whose nonlinear contribution coincides with that of the DBR. It should be noticed that the nonlinear length L_{NL} is twice the field penetration depth inside the DBR, which indicates the real reflection point of the light in the DBR and whose expression was derived in (Melloni *et al.* 2003d). In strong gratings L_{NL} is independent of the physical length L of the grating itself and in this condition both L_{NL}^{+} and L_{NL}^{-} approaches $L_{\mathrm{NL}}/2$.

When nonlinear DBRs are cascaded to build up a SWS, the above described NEC can be directly used to replace each single Fabry–Pérot cav-

ity with an equivalent cavity, as shown in Fig. 2b. The equivalent length $L_{r,i}$ of the ith cavity is simply $L_{r,i} = L_{\mathrm{e},i} + L_{\mathrm{c},i} + L_{\mathrm{e},i+1}$ with $L_{\mathrm{e},i}$ and $L_{\mathrm{e},i+1}$ the equivalent length of the two DBRs forming the cavity and $L_{c,i}$ the distance between the two DBRs. To include the Kerr nonlinearity in the equivalent cavities, it is convenient to define an equivalent nonlinear refractive index inside each cavity,

$$n_{2\mathrm{e},i} = n_2 \frac{L_{\mathrm{NL,i}} + 2L_{\mathrm{c},i} + L_{\mathrm{NL,i+1}}}{2L_{\mathrm{r},i}}, \tag{16}$$

where $L_{\mathrm{NL},i}$ and $L_{\mathrm{NL},i+1}$ are the nonlinear length of the two DBRs of the i-cavity. The parameter $n_{2\mathrm{e},i}$, which is the value of the nonlinear refractive index to be used in the NEC model, also depends on the geometrical length of the cavity.

3.3.2. *Time-domain simulation of the equivalent SWS*

Once every DBR is replaced by its NEC, an equivalent SWS is obtained which consists of equivalent cascaded cavities with geometrical length L_{r} and coupled by dimensionless mirrors with field reflectivity r. Each equivalent cavity is filled with a homogeneous medium with linear refractive index n_a and an equivalent nonlinear index $n_{2,\mathrm{e}}$. After the transformation into the equivalent SWS, the time-domain numerical solver described in Melloni *et al.* (2003b) can be straightforwardly used. This method is based on the fact that both the forward wave A^+ and the backward wave A^- inside each cavity obey to the coupled Nonlinear Schrödinger Equations (NLSE), which in the absence of material dispersion reduce to (Agrawal 1999)

$$\pm j \frac{\partial E^{\pm}}{\partial z} = -\frac{j}{2}\alpha E^{\pm} + \gamma |E^{\pm}|^2 E^{\pm} - 2\gamma |E^{\mp}|^2 E^{\pm}, \tag{17}$$

where α includes propagation losses (or gain), γ is the nonlinear propagation constant proportional to n_2 and the last term refers to the XPM contribution due to the counterpropagating wave. In most cases material dispersion can be neglected because the SWS dispersion is typically several order of magnitude higher and the coupled NLSEs reduces to the ordinary differential equations written in Equation (17), directly integrable by means of conventional numerical techniques. However, in all cases where material dispersion must be included, a split-step Fourier method can be applied as an extension of the proposed method (Agrawal 1999).

Two main advantages of the proposed method can be pointed out with respect of conventional time-domain methods. First of all, this approach permits to separate the nonlinear propagation inside each resonator from

the linear coupling at the resonator interfaces. In fact, the equivalent SWS is divided into a number of subcells, a number of which, equal to the number of the DBRs, include a concentrated mirror, fully described by its linear transfer matrix; all the remaining subcells consist of portions of homogeneous material with equivalent nonlinear index $n_{2e,i}$, given by Equation 16. Second, since the medium filling the cavity is homogeneous, the sampling step to be used in the computation is no more imposed by the DBR period. The minimum number of subcells has to be fixed in order to satisfy the Nyquist sampling theorem, that is the inverse of transit time across a subcell must be higher than twice the maximum frequency of the input signal. It should be noticed that the reduction of the required computational time with respect to conventional techniques is as much higher as the SWS cavities are longer than the DBR. In all the results shown in Section 5 no more than two subcells per cavity were used in the computation.

4. Frequency-domain methods

In this section, two frequency-domain methods are described, being respectively a fast solution of Maxwell's equations after a suitable transformation into a nonlinear directly integrable system (NI-FD) and an iterative algorithm based on a nonlinear extension of the Eigen-Mode Expansion (EME) method.

4.1. NUMERICAL INTEGRATION OF MAXWELL EQUATIONS IN THE FREQUENCY-DOMAIN (NI-FD)

In this section a simple and fast technique for one-dimensional nonlinear problems is discussed. The Maxwell equations are transformed into a new system which, in the case of lossless structures, can be decoupled and easily integrated. The technique does not use any approximations and its efficiency does not depend on nonlinearity level. Here only the main features are described, more details can be found in (Petráček 2006).

The Maxwell equations in the frequency-domain can be written as

$$\frac{\mathrm{d}}{\mathrm{d}z}E_x(z) = -jkcB_y(z), \tag{18}$$

$$\frac{\mathrm{d}}{\mathrm{d}z}\left[cB_y(z)\right] = -jkn^2(z, |E_x|^2)E_x(z), \tag{19}$$

where $k = \omega/c$ is the vacuum wavenumber and $n(z, |E_x|^2)$ is the refractive index profile given by Equation 1.

Assuming wave incidence only from the left side of the structure, electric fields in the semi-infinite outer spaces [with the refractive indices $n(0-)$ and $n(L+)$] can be expressed as

$$E_x(z<0) = A_{\text{in}} \exp[-jkn(0-)z] + A_{\text{ref}} \exp[jkn(0-)z], \tag{20}$$

$$E_x(z>L) = A_{\text{out}} \exp[-\text{j}kn(L+)(z-L)], \tag{21}$$

where A_{in}, A_{ref}, and A_{out} are the complex amplitudes of the electric field incident, reflected and transmitted by the structure, respectively.

Now, by defining a normalized wave admittance q and its reciprocal normalized wave impedance p (see e.g. Kuester and Chang 1975)

$$q \equiv p^{-1} \equiv -\frac{jcB_y}{E_x} \tag{22}$$

the Maxwell equations (18) and (19) are transformed as

$$\frac{\text{d}}{\text{d}z} q(z) = -k\left[q^2(z) + n^2\left(z, |E_x|^2\right)\right], \tag{23}$$

$$\frac{\text{d}}{\text{d}z} p(z) = k\left[1 + p^2(z)\, n^2\left(z, \left|pcB_y\right|^2\right)\right]. \tag{24}$$

Note that q and p can diverge and therefore during the numerical integration it is necessary to alternate between the two equations.

Here only the solution of Equation (23) will be considered as Equation (24) can be treated in similar manner. For lossless structures, $|E_x(z)|^2$ is calculated from the power flux conservation law

$$|E_x(z)|^2 \text{Im}[q(z)] = -|A_{\text{out}}|^2 n(L+) \tag{25}$$

and subsequently used in Equation (23). Boundary conditions for q are straightforward to derive,

$$q(0) = \text{j}n(0-)\frac{r-1}{r+1}, \tag{26}$$

$$q(L) = -\text{j}n(L+), \tag{27}$$

where $r \equiv A_{\text{ref}}/A_{\text{in}}$. These conditions constitute the two-point boundary value problem for q, and an efficient solution technique, namely "shooting method," can be formulated to solve Equation (23). The technique uses (27) as the initial condition for numerical integration of (23) [or (24)] and iteratively searches for A_{out}.

Note that during the calculation only one first order differential equation is solved and therefore the method is about twice faster than techniques based on direct integration of Equations (18) and (19).

4.2. NONLINEAR EXTENSION OF THE EME (NEME-FD)

In this section, a nonlinear extension (Maes *et al.* 2004) to the frequency-domain eigenmode expansion solver (Cavity Modelling Framework (CAMFR), website in the References) is used (NEME-FD). Eigenmode expansion techniques start out by slicing up the structure into layers in which the index profile does not change in the propagation direction (Fig. 3). In each of these layers, any optical field can be written as a sum of eigenmodes, which are the natural field profiles of the layer. The linear properties of the complete structure can then be calculated by stitching the eigenmodes of the different layers together using scattering matrices, which describe the transmission and reflection of each mode at the interface between two layers.

In the presence of the Kerr effect, the field dependence of the index profile has to be taken into account, according to Equation (1). As a result, the refractive index will not be constant anymore in each layer of Fig. 3. Therefore, according to the spatial profile of $E(z)$, each of the layers is further subdivided in a set of sublayers (Fig. 4), in which the total refractive index is taken to be constant again.

To determine the optical field and therefore the total refractive index, an iterative method is used. Starting from a certain index distribution, e.g., the linear distribution or a previously calculated approximate solution, a lin-

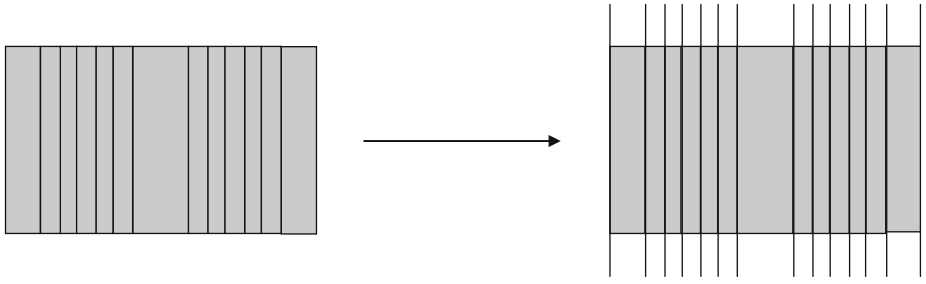

Fig. 3. Discretization of a one-dimensional resonator structure in (linear) layers which are invariant in the propagation direction.

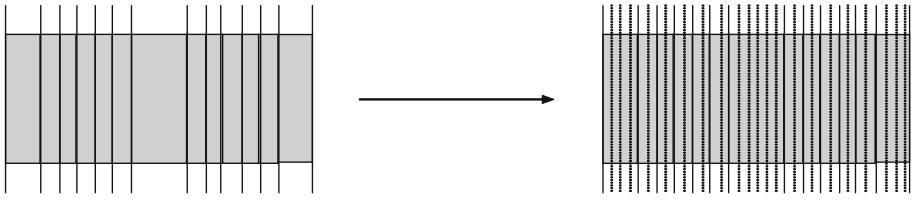

Fig. 4. Additional discretization of each layer in a set of sublayers.

ear eigenmode calculation is performed, giving the field profile $E(z)$ of the complete structure. With the value of the optical field in the center of each nonlinear layer, the total refractive index n_i of each nonlinear layer calculated at iteration step i is updated with a new value n_{i+1} according to Equation (1). This process is repeated until convergence is obtained.

The accuracy of the obtained solution is then determined by the number of subdivisions of each linear layer and by the convergence parameter $\varepsilon = |n_{i+1} - n_i|$. In the case of a standing-wave resonator, the number of subdivisions must be much larger than in the case of a simple waveguide as the spatial fluctuations of $|E(z)|^2$ are much faster. For multiple cavities and/or higher input fields, it becomes more and more difficult to obtain convergence. In this case, the new value n_w of the refractive index is calculated as a weighted average of the two values, namely

$$n_{w,i+1} = \frac{n_{i+1} + \beta n_i}{1 + \beta} \tag{28}$$

with $\beta > 0$. In this way, the higher is the β value, the less abrupt the intermediate solution is changed and convergence is obtained in a slower, but smoother way.

5. Numerical results

A comparative numerical analysis of self-phase modulation effects in SWSs has been carried out by using the methods described in Sections 3 and 4.

As a first example, we considered a SWS with the structure shown in Fig. 1 made of $N = 2$ cavities with optical length $\lambda_0 = 1550\,\text{nm}$ coupled by an intermediate $\lambda_0/4$ cavity. The calculated amplitude reflection and transmission coefficients of the DBRs described in Section 2 are $r = 0.9893\exp[\text{j}\phi(\lambda)]$ and $t = -\text{j}0.1456\exp[\text{j}\phi(\lambda)]$ with $\phi(\lambda) = 19.7088(\lambda - 1.55)$, λ being the wavelength in micron unit. Figure 5 shows the transmission (a) and the group delay (c) of the double cavity in the case of increasing normalized input power $n_2 I$. Due to the positive ($n_2 > 0$) Kerr effect, the SWS spectrum is as much shifted to the right as the nonlinearity level is increased and at sufficiently high input power level bistability effects occur for $\lambda > \lambda_0$. Fig. 5b, d shows a detail of the frequency range between 1,550.5 and 1,550.7 nm. It should be noticed that the group delay is strongly enhanced at the frequencies where bistable transitions occur: as shown in Fig. 5b and Fig. 5b, the agreement of the compared data is reduced at these points that are the most critical to be calculated in both time and frequency-domain methods.

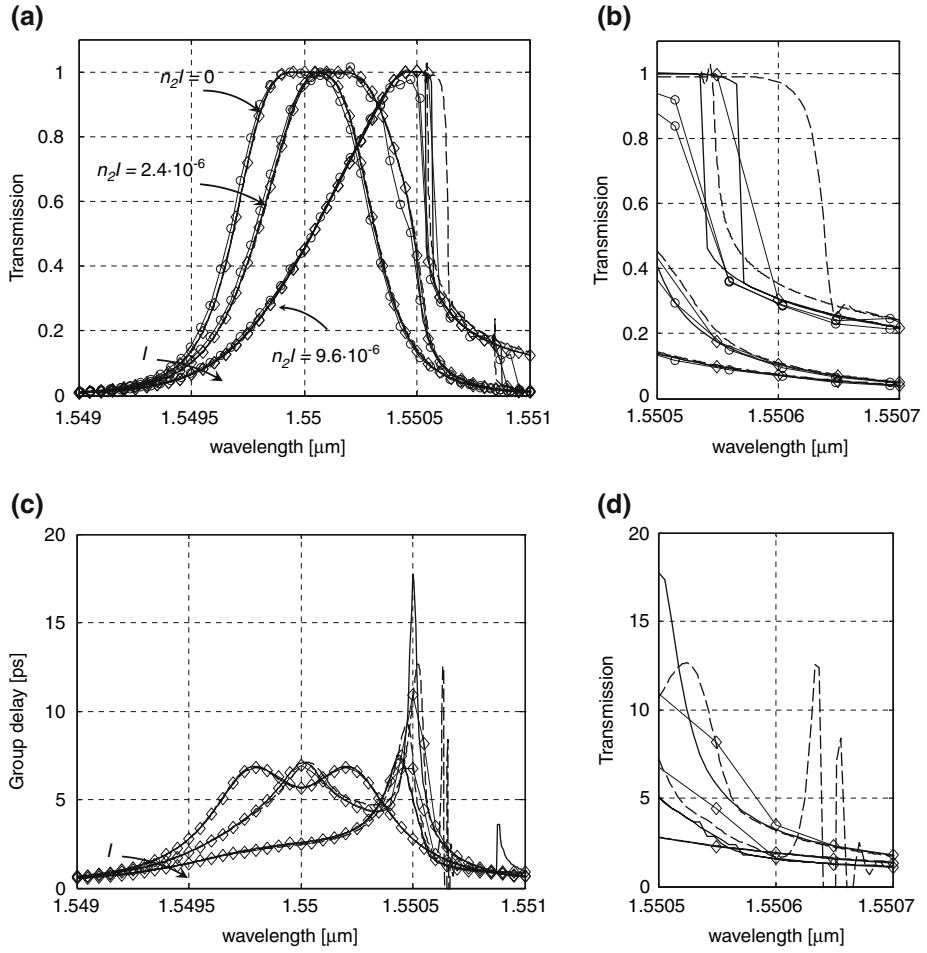

Fig. 5. Transmission (a–b) and group delay (c–d) of a double cavity SWS for increasing values of the input power. The frequency range between 1550.5 and 1550.7 nm, where bistability effects occur, is expanded in (b) and (d). Data shown in the figure are calculated by NI-FD (solid lines), NEC-TD (dashed lines), PVC-FDTD (diamonds) and LM-FDTD (circles, group delay not available). Data obtained by NEME-FD are not distinguishable from NI-FD in the scale of the figure.

For the NEC-TD method, the parameters of the equivalent cavities were calculated. Since the transmission bandwidth of the SWS (< 1 nm) is much narrower than the reflection bandwidth of the DBR (> 140 nm), it is possible to further simplify the equivalent circuit of the DBR by assuming a wavelength independent equivalent length $L_e = 1.4492\,\mu$m, responsible for the wavelength dependent phase shift $\phi(\lambda)$, and by adding a constant phase shift $\phi_0 = 4\pi n_a L_e/\lambda_0 = 30.5486$ rad to each concentrate reflector. The nonlinear equivalent length, calculated using Equation (15) is $L_{NL} = 1.573\mu$m for every grating, whereas the nonlinear equivalent refractive index, calculated

with Equation (16) is $n_{2e,1} = n_{2e,3} = 0.62n_2$ in the λ_0 cavities and $n_{2e,2} = 0.566n_2$ in the central $\lambda_0/4$ cavity. To evaluate the nonlinear spectral response of Fig. 5 an optical signal with constant intensity I and linearly time varying wavelength, from 1.49 to 1.51 nm, was positioned at $z = 0$ and the output complex amplitude was acquired. In order to avoid distortion in the calculated spectrum, the change of the input wavelength must occur on a time scale longer than group delay of the SWS. Thanks to the removal of the DBR, only two points per cavity were used in all the simulations shown in this section.

In the LM-FDTD method, parameters $\omega_r = 0.8 \times 10^{-16}$ rad/s, $\gamma_0 = 4 \times 10^5\,\mathrm{s}^{-1}$, $\epsilon_\infty = 1$ have been used. The ϵ_S values that give $n_a = 2.6$ and $n_b = 2.36$ at $\lambda_0 = 1550$ nm are 6.6147 and 5.4588, respectively. In this conditions it is assured that Kerr effect is predominant because the phase mismatch $\Delta k = 3k(\omega) - k(3\omega)$ of third harmonic generation, which is the most intense secondary conversion process, in the frequency range of interest is kept sufficiently high by material dispersion. The input signal is a continuous wave at a given frequency and the transmitted power at every wavelength is collected after simulation has completed the transient (group delay was not calculated by LM-FDTD). The FDTD grid step is 15 nm, as a compromise between high spatial resolution (21 cells per Bragg grating period and 40 cells per cavity) and reasonable computational effort. The numerical domain consists of 2305 cells (34.57 μm) in the double cavity case and 3462 (51.94 μm) in the triple cavity one. As an effect of the discretized grid, an artificial shift in the position the resonant frequency, fixed by the cavity length, was found, with an uncertainty of ± 7.5 nm (half spatial step). In the figures, data have been centered at the correct wavelength to allow a better comparison with the other proposed methods. Since numerical dispersion is compensated (see Section 3.2), the only source for this inaccuracy is the spatial grid discretization, assumed constant in the whole computational domain. A finer grid would partially increase the accuracy of the result, but with significantly higher computational efforts. A more efficient solution is to use a nonuniform grid to have a better representation of the index discontinuity at the interface between the two materials and to compensate for the numerical dispersion originated by the nonuniform grid by using a PVC approach.

In the PVC-FDTD method, no artificial shift of the SWS spectrum is generated by the grid discretization, thanks to the phase velocity corrected scheme. Only a slight change in the bandwidth can occur if the discretization is not sufficiently accurate. However, in the example reported in the paper, where 72 points per λ/n_0 (with n_0 being equal to n_a or n_b) were used, this effect is negligible. To give an idea of the magnitude of this numerical artifact, the linear spectral response the double cavity SWS of

Fig. 5 was calculated also with a grid discretization reduced down to 24 points per λ/n_0 and a bandwidth variation of 0.05 nm was found.

In the NEME-FD method, 16 divisions per wavelength λ/n_0 have been used. Values of the β parameter up to 8 are required to obtain convergence for a convergence parameter $\varepsilon = 10^{-5}$. The nonlinear solution is calculated with a frequency sweep, starting from regions where no bistability occurs and moving towards the critical regions. The nonlinear result calculated at each wavelength is used as starting point of the NEME-FD algorithm for the next wavelength. The upper and lower arms of the bistable region of Fig. 5 are obtained by sweeping upward and downward, respectively, the wavelength axis.

Figure 5 shows that all the proposed methods are in very good agreement in the left side of the spectrum even for high nonlinearity. On the right side, where sharp transitions of the spectrum versus frequency occur, time-domain approaches look less accurate. In the case of the LM-FDTD bistability is not observed, while in the NEC-TD method the width of the bistabile region is wider than that calculated by frequency-domain methods (NEME-FD and NI-FD). In case of $n_2 I = 9.6 \times 10^{-6}$ the width of the calculated bistability regions are 0.028 and 0.082 nm respectively. This effect is due to the presence of a very high peak in the group delay (see Fig. 5d) which imposes a very slow variation in the carrier frequency of the input signal to accurately reconstruct the spectral response. These sharp transitions have also the effect to slow down convergence of both the NI-FD and NEME-FD frequency-domain methods, which however show the best agreement in the entire spectral range and are not distinguishable in the scale of Fig. 5.

Even though frequency-domain methods are the best candidates to reconstruct the nonlinear spectral response of SWSs, in the nonlinear regime some effects could arise that strictly require a time-domain investigation to be observed. To this aim, Fig. 6 shows the transmission (a) and group delay (b) of a SWS made of $N = 3$ coupled resonators. The good agreement of all the methods in the left-hand side of the spectrum is confirmed, but when the nonlinearity increases to $n_2 I = 5.4 \times 10^{-6}$ different behaviors appears in the right-hand side. The NI-FD provides solutions for all wavelengths, the iterative NEME-FD does not converge for some values of $\lambda > 1.5505\,\mu$m and all time-domain methods reveal anomalous oscillations in the SWS spectrum. The origin of such spectral oscillations can be better understood by looking at the time-domain simulations shown in Fig. 7. In such conditions a continuous input signal In at $\lambda = 1.5506\mu$m breaks into a stable periodic pulse train Out. Simulations were performed at two different input power level, $n_2 I = 5.4 \times 10^{-6}$ and $n_2 I = 9.6 \times 10^{-6}$, and both transmission (a) and (c), and reflection, (b) and (d), time responses have been compared. In the case of LM-FDTD (dotted lines) a longer rise time

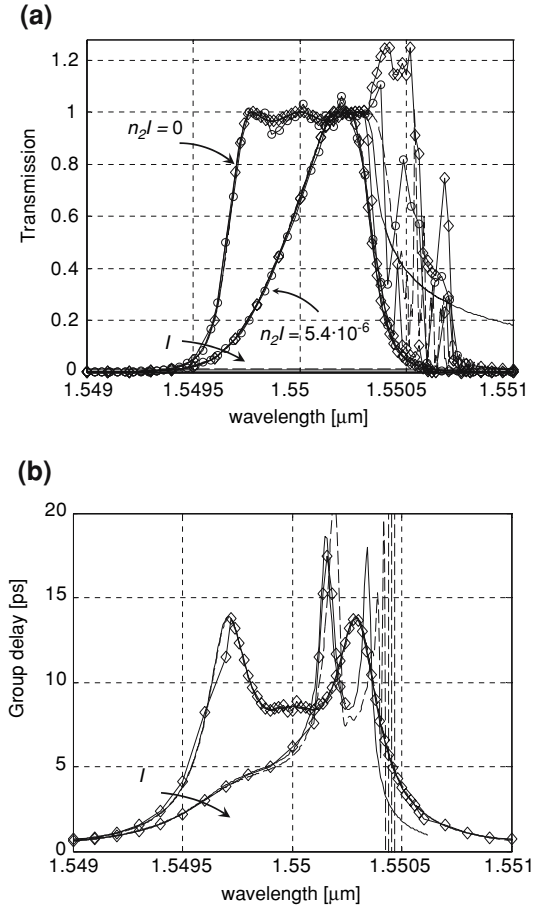

Fig. 6. Transmission (a) and group delay (b) of a triple cavity SWS for increasing values of the input power. Data shown in the figure are calculated by NI-FD (solid lines), NEC-TD (dashed lines), PVC-FDTD (diamonds) and LM-FDTD (circles, group delay not available). Data obtained by NEME-FD are not distinguishable from NI-FD in the scale of the figure.

for the input signal was used to investigate its impact on the output signal. After the initial transient, a good agreement among all the compared time-domain methods is reached, showing that the transient profile of the input signal does not affect neither the shape, nor the amplitude and repetition rate of the pulse train. Once the steady state is reached, the periodic pattern only depends on the frequency detuning of the input signal with respect to the SWS resonant frequency λ_0 and on the nonlinearity $n_2 I$. Therefore, this phenomenon can be considered a *self-pulsing* effect in the SWS. Self pulsing in optical resonators has been investigated extensively in literature (Lugiato 1980). In this conditions the group delay loses its physical meaning of transit time of an input signal across the device and this justifies the deep oscil-

lations in the spectrum reported in Fig. 6. In the example reported in the figure, pulse repetition rate is about 30 ps for $n_2 I = 5.4 \times 10^{-6}$ and 40 ps for $n_2 I = 9.6 \times 10^{-6}$.

6. Discussion and conclusion

A comparison of the computational efficiency of the presented methods is provided in this concluding section. However, it is worthwhile to stress that the following discussion is intended to give only an order of magnitude for the performance of the proposed approaches. Several different factors, related to the architecture of hardware platforms, to the specific software implementation (compilers, libraries) and also to the requested precision in the results have all a direct influence and can significantly affect computational time. Therefore, the figures of merit defined in this section are used as rough indicators to point out some general features, advantages and limitations, of the proposed methods.

The nonlinear spectral responses shown in Figs. 5 and 6 were obtained either by using frequency-domain and time-domain methods. We define F_{f} as the number of calculated spectral points, in pm unit, normalized to CPU time (s) and CPU frequency (GHz). As shown in Table 1 frequency-domain methods are typically more efficient than time domain methods (nearly two order of magnitude in the examples reported in the paper). The main limitation of the NEC-TD is the need for a very slow change of the input wavelength to reduce artificial distortion in the calculated spectrum, especially at the frequencies where sharp transitions occurs and the group delay is maximum. It should be also noticed that the LM-FDTD is less computational efficient than nondispersive models, but it allows to take into account the physics of real materials and can also include nonlinearity to every order.

With respect to time-domain simulations shown in Fig. 7, we define a figure of merit F_t as the number of calculated temporal points, in ps unit normalized to CPU time (s) and CPU frequency (GHz). Moreover some considerations on the number of spatial points N_z used to sample the structure are added. In PVC-FDTD a nonuniform mesh with 72 points per λ/n_0 is used, which lead to $N_z = 6040$ spatial samples along the SWS. In LM-FDTD the 15 nm grid step gives $N_z = 3460$, while in the NEC-FDTD only 10 spatial points are required for the triple cavity SWS. As shown in Table 1, PVC-FDTD has twice the points of LM-FDTD, but a three times higher F_t factor is found, thus demonstrating a higher speed of the computational method. The higher F_t factor of the NEC-TD is entirely due to the extremely coarse sampling allowed by the equivalent circuit of the DBR. However, for the NEC-TD the increase in the factor F_t is much

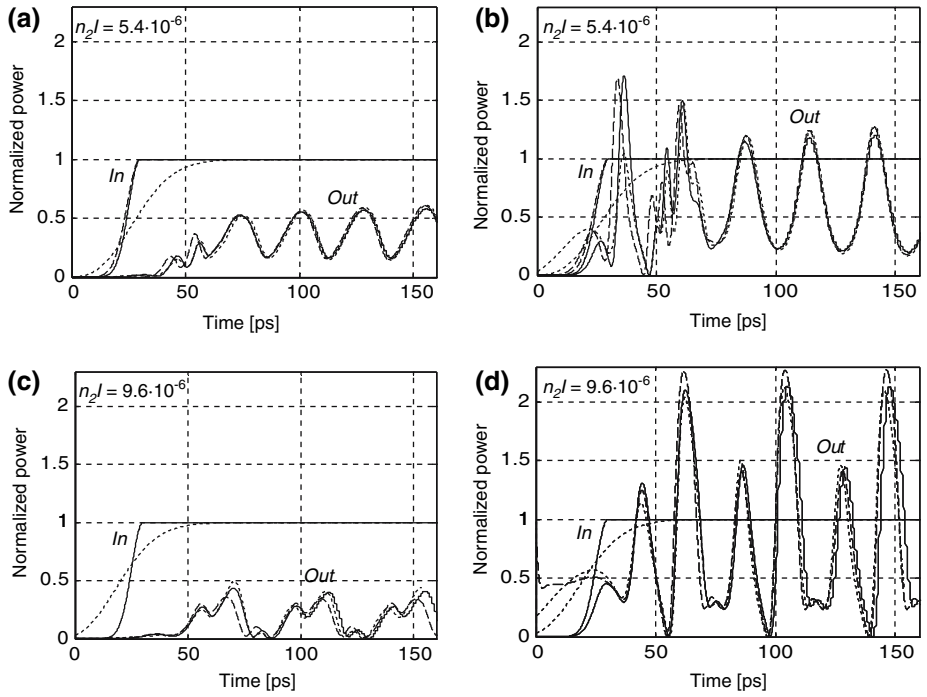

Fig. 7. Time-domain observation of self-pulsing effects in a triple cavity SWS at $\lambda = 1.5506\,\mu$m calculated by PVC-FDTD (*solid lines*), LM-FDTD (*dotted lines*) and NEC-TD (*dashed lines*). Transmission (a) and reflection (b) for $n_2 I = 5.4 \times 10^{-6}$ and transmission (c) and reflection (d) for $n_2 I = 9.6 \times 10^{-6}$ are shown.

lower than expected from the spatial sampling reduction. The main reason is that the computational speed of the nonlinear TD solver described in Section 3.3.2 is not optimized for the analysis of SPM effects in SWSs and conventional algorithms for partial derivatives differential equations are employed to include also the effect of gain (or loss) and frequency mixing phenomena. On the basis of these results, by combining the potentialities of the proposed methods in terms of minimum spatial sampling (given by NEC) and maximum computational speed per spatial point (given by PVC-FDTD), a rough estimate gives only 6 s CPU time to obtain each curve of Fig. 7 (160 ps) with a 3 GHz CPU frequency.

In conclusion, a detailed investigation of SWSs in Kerr nonlinear regime has been reported. A good agreement was found in the evaluation of the SWS nonlinear spectral response by using the numerical methods described in the paper, even when bistability and self-pulsing phenomena occur. Time-domain methods are less accurate to reconstruct the spectrum where sharp transitions versus frequency occur, as it happens in the case of bistable states. In fact at the boundary of the bistable regions strong peaks

Table 1. Computational efficiency of the proposed methods

Method	$F_f\left[\frac{pm}{sGHz}\right]$	$F_t\left[\frac{ps}{sGHz}\right]$	N_z
NI-FD	11.5	–	–
NEME-FD	2.5	–	–
PVC-FDTD	–	0.014	6040
LM-FDTD	0.05	0.004	3460
NEC-TD	0.025	0.05	10

occur in the group delay, which impose to largely increase simulation time to reach the same accuracy as given by frequency-domain methods. However, frequency-domain methods cannot easily reveal the regions in which stable solutions do not exist. For a sufficiently high number of cavities ($N = 3$ in the example reported in the paper) and high nonlinearity, self-pulsing phenomena are predicted by time-domain methods only. From this comparison, lasted three years in the frame of COST P11, it appears that a single numerical method is not sufficient to fully and effectively characterize a SWS in the nonlinear regime, but a comparative analysis including both time-domain and frequency-domain methods is necessary for an accurate investigation. It has been also demonstrated that effective models based on equivalent circuits of optical structures can be exploited to greatly reduce the computational efforts of conventional numerical methods. The extension of the proposed analysis to the case of structure including material with gain or loss and chromatic dispersion is in progress and is let to a future contribution.

Acknowledgments

This work was carried out within Working Group 2 of European Action COST P11. The work of J.P. was supported by the Ministry of Education, Youth and Sport of the Czech Republic (OC P11.002).

References

Absil, P.P., J.V. Hryniewicz, B.E. Little, P.S. Cho, R.A. Wilson, L.G. Joneckis and P.T. Ho. *Opt. Lett.* **25** 554, 2000.
Agrawal, G.P. *Nonlinear Fiber Optics*. Academic Press, New York, 1999.
Blair, S. *Opt. Exp.* **13** 3868, 2005.
Boyd, R.W. *Nonlinear Optics*. Academic Press, New York, 1992.
CAMFR, http://camfr.sourceforge.net
Chen, Y., G. Pasrija, B. Farhang-Boroujeny and S. Blair. *Opt. Lett.* **28** 1945, 2003.
Christ, A., J. Fröhlich and N. Kuster. *IEICE Trans. Commun.* **E85-B** 2904, 2002.

Heebner, J.E., N.N. Lepeshkin, A. Schweinsberg, G.W. Wicks, R.W. Boyd, R. Grover and P.T. Ho. *Opt. Lett.* **29** 769, 2004.
Joseph, R.M. and A. Taflove. *IEEE Trans. Antennas Propag.* **45** 364, 1997.
Kuester, E.F. and D.C. Chang. *IEEE Trans. Microwave Theor. Tech.* **MTT-23** 98, 1975.
Lauritano, M., A. Parini, G. Bellanca, S. Trillo, M. Conforti, A. Locatelli and C. De Angelis. *J. Opt. A: Pure Appl. Opt.* **8** S494, 2006.
Lugiato, L.A. *Opt. Commun.* **33** 108, 1980.
Maes, B., P. Bienstman and R. Baets. *Opt. Quantum. Elect.* **36** 15, 2004.
Melloni, A., F. Morichetti and M. Martinelli. *Opt. Phot. News* **44**, 2003a.
Melloni, A., F. Morichetti and M. Martinelli. *Opt. Quantum Elect.* **35** 365, 2003b.
Melloni, A., F. Morichetti, S. Pietralunga and M. Martinelli. In: *Proceeding of the 11th European Conference on Integrated Optics*, Prague, 2003c, p. 97.
Melloni, A., M. Floridi, F. Morichetti and M. Martinelli. *J. Opt. Soc. Am. A* **20** 273, 2003d.
Petráček, J. *Opt. Comm.* **265** 331, 2006.
Stignani, S. *Graduation Thesis*. Politecnico di Milano, 2001.
Taflove, A. *Computational Electrodynamics: The Finite Difference Time Domain Method for Electromagnetics*. Artech House, Boston, 1995.
Xu, Y., R.K. Lee and A. Yariv. *J. Opt. Soc. Am. B* **17** 387, 2000.
Yariv, A., and P. Yeh. *Optical Waves in Crystals*. Wiley John, & Sons, (1984).
Yee, K.S. *IEEE Trans. Antennas Propag.* **14** 302, 1966.